GUIDANCE, NAVIGATION AND CONTROL FOR ASTEROID ORBIT STATION-KEEPING WITH IN-SITU GRAVITY ESTIMATION

Julio C. Sanchez[(1)]**, Rafael Vazquez**[(1)]**, James D. Biggs**[(2)]**, Franco Bernelli-Zazzera**[(2)]

[(1)] *Universidad de Sevilla, Sevilla, Spain, 41008, {jsanchezm@us.es; rvazquez1@us.es}*
[(2)] *Politecnico di Milano, Milano, Italy, 20133 {biggs_james@yahoo.co.uk;*
franco.bernelli@polimi.it}

ABSTRACT

This manuscript explores the concept of model-learning predictive control for orbit-attitude station-keeping in the vicinity of an asteroid. The asteroid gravity field inhomogeneities are assumed to be unknown a priori. In order to infer the gravity model parameters, these are simultaneously estimated with the state through an unscented Kalman filter. The progressive gravity model identification is combined with a model-learning predictive control strategy. The predictive control scheme increases its accuracy since the model parameters are estimated in-situ. Consequently, the tracking errors decrease over time as the model accuracy increases. Numerical results are shown and discussed, comparing the learning-based MPC strategy to a more classical non-learning approach to demonstrate the benefits and trade-offs of the former with respect to the latter.

1 INTRODUCTION

Small bodies exploration can enable a deeper understanding of the early solar system and planetary processes [1]. Future exploration missions are aiming to explore Jupiter trojan asteroids (Lucy) and metallic objects (Psyche). Additionally, the asteroid deflection proof mission DART will impact a spacecraft on the asteroid moon (Didymoon) of the binary system 65803 Didymos.

Due to their inhomogenous gravity fields, asteroids generate a complex dynamical environment in their vicinity. This yields large deviations with respect to simplified Keplerian dynamics [2]. For example, a Keplerian closed orbit may unstabilize into a collision or escape trajectory. As a consequence, the design of stable orbits (e.g. frozen orbits) has received considerable attention in the literature [3, 4, 5]. However, these works assumes simplified gravity and solar radiation pressure (SRP) models, thus requiring active closed-loop tracking control in order to maintain its orbit. In that line, model predictive control (MPC) [6] may be a suitable closed-loop control option in an optimal manner (e.g. see [7] for MPC-based low Earth orbits station-keeping).

The navigation process around non-visited small bodies is challenging since limited data of the body (orbit, spin-rate and pole orientation) is known prior to the gravitational capture. In terms of orbit operations, the main uncertainty source cames from the inhomogenous gravity field. Recent works are analyzing the feasibility of in-situ gravity field estimation. To this end, [8] employed optical navigation and satellite-to-satellite radiometric measurements for gravity field determination. An extended state observer with a regression process was designed in [9] to infer gravity parameters and solar sail degradation. Unscented Kalman filtering (UKF), developed by [10], has been widely employed for asteroid navigation in [11, 12, 13] while [14] extended previous works by including the gravity field estimation.

Asteroid navigation devices, such as cameras or LIDAR, usually rely on relative measurements with respect to asteroid surface landmarks. As a consequence, the spacecraft orientation shall guarantee line-of-sight with the asteroid surface for these devices [15, 16]. In this context, orbit-attitude dynamics is coupled due to the gravity-gradient torque [17]. This torque depends on the spacecraft position and orientation with respect to the orbit frame. The attitude dynamics in the vicinity of asteroids may alter passive gravity-gradient stabilization domains [18]. Under the previous consideration, active closed-loop control has to be considered in order to ensure a proper pointing of sensors.

Taking into consideration the previous facts, this paper presents an integrated model-learning predictive GNC strategy for orbit-attitude station-keeping in the vicinity of asteroids. Closed-loop control is achieved through the novel paradigm of model-learning predictive control [19]. In that line, UKF-based navigation is employed to obtain a joint estimation of the state and gravity model parameters. The guidance and control is MPC-based and benefits from the UKF recursive in-situ learning of the gravity model, thus increasing its accuracy. The whole strategy follows the concept of tackling model uncertainty by inferring model parameters.

The structure of the paper is as follows. Section II introduces the orbit-attitude dynamics in the vicinity of an asteroid. Section III presents the GNC scheme and its modules. Section IV shows numerical results from the comparison of the presented learning-based MPC with respect to a classical non-learning scheme. Finally, Section V concludes the paper with some remarks.

2 ORBIT-ATTITUDE DYNAMICS IN THE VICINITY OF AN ASTEROID

In this section, the orbit-attitude dynamics in the vicinity of an asteroid is presented. The main body is assumed to be uniformly rotating around its major inertia axis which this is the usual case for the majority of asteroids. Let denote the asteroid-centered inertial frame as $I \equiv \{\mathbf{0}, \mathbf{i}_I, \mathbf{j}_I, \mathbf{k}_I\}$ being the asteroid center of mass its origin. Let denote the asteroid-centered rotating frame as $A \equiv \{\mathbf{0}, \mathbf{i}_A, \mathbf{j}_A, \mathbf{k}_A\}$ where $\mathbf{k}_A$ is aligned with the major inertia axis while $\mathbf{i}_A$ and $\mathbf{j}_A$ are contained on the equatorial plane. The frame A rotates with angular velocity $\boldsymbol{\omega}_{A/I} = \omega_T \mathbf{k}_A$ ($\omega_T \equiv$ constant) with respect to the inertial frame. Let denote the orbit frame as $O \equiv \{\mathbf{r}, \mathbf{i}_O, \mathbf{j}_O, \mathbf{k}_O\}$ which evolves along the satellite orbit $\mathbf{r}$. The term $\mathbf{i}_O$ is the radial component (positive outwards the main body), $\mathbf{k}_O$ the normal component (parallel to the spacecraft angular momentum) and $\mathbf{j}_O$, the tangential component, completes the right-handed system. Finally, let denote the spacecraft body and camera frames as $B \equiv \{\mathbf{r}, \mathbf{i}_B, \mathbf{j}_B, \mathbf{k}_B\}$ and $C \equiv \{\mathbf{r}, \mathbf{i}_C, \mathbf{j}_C, \mathbf{k}_C\}$ respectively. The camera boresight is aligned with the $\mathbf{k}_C$ direction. These frames of reference are depicted in Fig. 1.

2.1 Orbital motion

This paper employs the modified equinoctial elements (MEE), see [20] for the details, for the orbit state representation $\mathbf{x}_{\text{orb}} = [p, f, g, h, k, L]^T$. This parameterization avoids the classic orbital elements, $\{a, e, \omega, i, \Omega, \nu\}$, singularities for circular ($e = 0$) and equatorial orbits ($i = 0°$, $180°$). However, retrograde equatorial orbits are still singular for the MEE. The Gauss variational equations (GVE) for the modified equinoctial elements are written as as $\dot{\mathbf{x}}_{\text{orb}} = \mathbf{f}_{\text{GVE}}(\mathbf{x}_{\text{orb}}, \mathbf{F}^O)$ [20], where $\mathbf{F}^O = [F_r^O, F_t^O, F_n^O]^T$ is the non-Keplerian acceleration expressed in the orbit frame O. This term is composed of natural perturbations and the thrusters control

$$\mathbf{F} = \underbrace{\mathbf{F}_{\text{grav}}}_{\text{inhomogeneous gravity}} + \underbrace{\mathbf{F}_{\text{sun}}}_{\text{Sun gravity}} + \underbrace{\mathbf{F}_{\text{SRP}}}_{\text{solar radiation pressure}} + \underbrace{\mathbf{F}_u}_{\text{control acceleration}}. \tag{1}$$
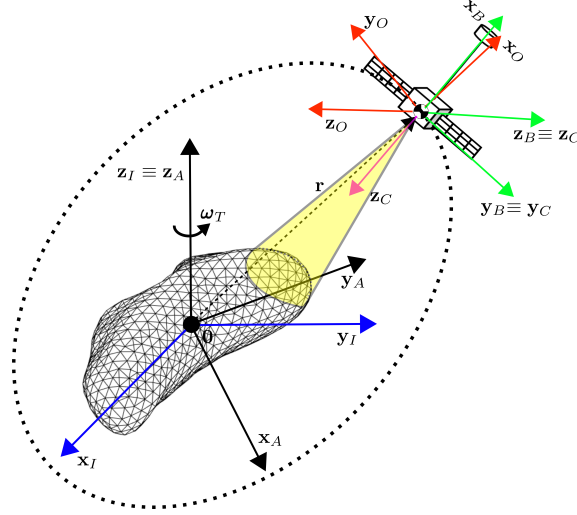
Figure 1: Inertial, asteroid, orbit, body and camera frames of reference.

2.1.1 Inhomogeneous gravity field

This is the most dominant term in a low asteroid orbit. In this work, the inhomogenous gravity field is modelled through the spherical harmonics expansion series [21]. As such, the non-Keplerian gravity is given by, see [22], the following series truncated at $i_{\max}$ degree and order

$$\mathbf{F}_p^S = \sum_{i=2}^{i_{\max}} \sum_{j=0}^{i} \frac{\mu}{r^2} \left(\frac{R_e}{r} \right)^i \begin{bmatrix} -(i+1)P_i^{(j)}(C_{ij}\cos(j\lambda) + S_{ij}\sin(j\lambda)) \\ \frac{j}{\cos\phi} P_i^{(j)}(-C_{ij}\sin(j\lambda) + S_{ij}\cos(j\lambda)) \\ \cos\phi P_i^{(j)'}(C_{ij}\cos(j\lambda) + S_{ij}\sin(j\lambda)) \end{bmatrix}, \tag{2}$$

where μ is the asteroid main gravitational parameter, $r = \|\mathbf{r}\|_2$ is the orbital radius, $\lambda = \arctan(y_A/x_A)$ is the longitude (measured counter clockwise in the equatorial plane $x_A y_A$) and $\phi = \arcsin(z_A/r)$ is the latitude. Note that Eq.(2) is expressed in the S frame. The S frame denotes the spherical frame as $S \equiv \{\mathbf{r}, \mathbf{i}_S, \mathbf{j}_S, \mathbf{k}_S\}$ with $\mathbf{i}_S$ being the radial direction, $\mathbf{j}_S$ pointing to the east and $\mathbf{k}_S$ to the north pole. The spherical harmonics coefficients C_{ij} and S_{ij} are normalized with respect to the normalization radius R_e (which is usually taken as the asteroid maximum elongation). The term $P_i^{(j)}$ is the ith degree normalized Legendre polynomial of the first kind in $\sin\phi$ and $P_i^{(j)'}$ is its first derivative with respect to $\sin\phi$. To insert the non-Keplerian gravity into the GVE, Eq.(2) has to be projected in the orbit frame as

$$\mathbf{F}_p(\mathbf{x}_{\mathrm{orb}}) = \mathbf{R}_I^O(\mathbf{x}_{\mathrm{orb}})\mathbf{R}_A^I \mathbf{R}_S^A(\lambda, \phi)\mathbf{F}_p^S(r, \lambda, \phi), \tag{3}$$

where $\mathbf{R}_S^A$ denotes the rotation matrix from the spherical to the asteroid frame, $\mathbf{R}_A^I$ is the rotation matrix from the asteroid to the inertial frame (it only depends on the asteroid rotation rate ω_T which is constant) and $\mathbf{R}_I^O$ denotes the rotation matrix from the inertial to the orbit frame. Note that $[r, \lambda, \phi]^T \equiv \mathbf{f}_{\mathrm{orb}}(\mathbf{x}_{\mathrm{orb}})$ where $\mathbf{f}_{\mathrm{orb}}(\mathbf{x}_{\mathrm{orb}}) : \mathbb{R}^6 \to \mathbb{R}^3$ is the mapping function between MEE and position coordinates in the asteroid frame.

2.1.2 Solar perturbations

The solar perturbations are the Sun gravity and its radiation pressure. The Sun gravity perturbation is

$$\mathbf{F}_{\text{sun}}(\mathbf{x}_{\text{orb}}) = \mathbf{R}_I^O(\mathbf{x}_{\text{orb}})\mu_\odot \left(\frac{\mathbf{r}_\odot - \mathbf{r}}{\|\mathbf{r}_\odot - \mathbf{r}\|_2^3} - \frac{\mathbf{r}_\odot}{\|\mathbf{r}_\odot\|_2^3} \right), \tag{4}$$

where $\mathbf{r}_\odot$ is the Sun position in the asteroid-centered inertial frame and $\mu_\odot = 1.3271244 \cdot 10^{11}$ km^3/s^2 its standard gravity parameter. The solar radiation pressure is considered in a simplified way as

$$\mathbf{F}_{\text{SRP}}(\mathbf{x}_{\text{orb}}) = -\mathbf{R}_I^O(\mathbf{x}_{\text{orb}})\frac{C_R p_{1\text{AU}} A}{m} \left(\frac{r_{1\text{AU}}}{r_\odot} \right)^2 \frac{\mathbf{r}_\odot - \mathbf{r}}{\|\mathbf{r}_\odot - \mathbf{r}\|_2}, \tag{5}$$

where C_R, A and m are the spacecraft reflectivity coefficient, exposed surface and mass respectively. The term $p_{1\text{AU}} = 4.5$ μPa is the SRP at $r_{1\text{AU}} = 1$ AU.

2.2 Rotational motion

In this paper, the modified Rodrigues parameters (MRP), see [23], $\boldsymbol{\sigma} = [\sigma_1, \sigma_2, \sigma_3]^T$ are employed to describe the spacecraft attitude. They are preferred over the classical quaternions since they do not need to account for the unit-norm constraint, thus easing optimization constraints. The MRP relation with the rotation axis $\mathbf{e}_{\text{rot}}$ and angle θ_{rot} is $\boldsymbol{\sigma} = \mathbf{e}_{\text{rot}} \tan(\theta_{\text{rot}}/4)$. Note that singularities arise when $\theta_{\text{rot}} = \pm 2\pi$. These singularities could be avoided by constraining $\theta_{\text{rot}} \in [-\pi, \pi]$ since $\{\mathbf{e}_{\text{rot}}, \theta_{\text{rot}}\} \equiv \{-\mathbf{e}_{\text{rot}}, 2\pi - \theta_{\text{rot}}\}$ represent the same attitude. The rotation matrix $\mathbf{R}$, as a function of the MRP, is given by

$$\mathbf{R}(\boldsymbol{\sigma}) = \mathbf{I} + \frac{8\boldsymbol{\sigma}^\times \boldsymbol{\sigma}^\times - 4(1 - \|\boldsymbol{\sigma}\|_2^2)\boldsymbol{\sigma}^\times}{(1 + \|\boldsymbol{\sigma}\|_2^2)^2}, \tag{6}$$

being $\boldsymbol{\sigma}^\times$ the cross-product matrix associated to a MRP, see [17]. The MRP atttitude composition rule is given by

$$\boldsymbol{\sigma}_0 \xrightarrow{\boldsymbol{\sigma}_{\text{rot}}} \boldsymbol{\sigma}_f, \quad \boldsymbol{\sigma}_f = \frac{(1 - \|\boldsymbol{\sigma}_{\text{rot}}\|_2^2)\boldsymbol{\sigma}_0 + (1 - \|\boldsymbol{\sigma}_0\|_2^2)\boldsymbol{\sigma}_{\text{rot}} + 2\boldsymbol{\sigma}_0 \times \boldsymbol{\sigma}_{\text{rot}}}{1 + (\|\boldsymbol{\sigma}_{\text{rot}}\|_2 \|\boldsymbol{\sigma}_0\|_2)^2 - 2\boldsymbol{\sigma}_{\text{rot}}^T \boldsymbol{\sigma}_0}. \tag{7}$$

The MRP attitude kinematics is $\dot{\boldsymbol{\sigma}} = \mathbf{C}(\boldsymbol{\sigma})\boldsymbol{\omega}/4$ where $\boldsymbol{\omega} = [\omega_1, \omega_2, \omega_3]^T$ is the body angular velocity with respect to the inertial frame I expressed in the body frame B. The matrix $\mathbf{C}$ is given by

$$\mathbf{C}(\boldsymbol{\sigma}) = \begin{bmatrix} 1 + \sigma_1^2 - \sigma_2^2 - \sigma_3^2 & 2(\sigma_1\sigma_2 - \sigma_3) & 2(\sigma_1\sigma_3 + \sigma_2) \\ 2(\sigma_1\sigma_2 + \sigma_3) & 1 - \sigma_1^2 + \sigma_2^2 - \sigma_3^2 & 2(\sigma_2\sigma_3 - \sigma_1) \\ 2(\sigma_1\sigma_3 - \sigma_2) & 2(\sigma_2\sigma_3 + \sigma_1) & 1 - \sigma_1^2 - \sigma_2^2 + \sigma_3^2 \end{bmatrix}. \tag{8}$$

Since landmark-based navigation requires sensors pointing towards the asteroid surface, the body orientation with respect to the orbit frame, $\boldsymbol{\sigma}_{B/O}$, is of interest, thus the kinematics equation can be modified accordingly [17]

$$\dot{\boldsymbol{\sigma}}_{B/O} = \frac{1}{4}\mathbf{C}(\boldsymbol{\sigma}_{B/O})\left[\boldsymbol{\omega} - \mathbf{R}(\boldsymbol{\sigma}_{B/O})\boldsymbol{\omega}_{O/I}^O(\mathbf{x}_{\text{orb}}) \right], \tag{9}$$

where $\boldsymbol{\omega}_{O/I}^O$ is the angular velocity of the orbit frame with respect to the inertial frame. In that line, let define the attitude state as $\mathbf{x}_{\text{att}} = [\boldsymbol{\sigma}_{B/O}^T, \boldsymbol{\omega}^T]^T$.
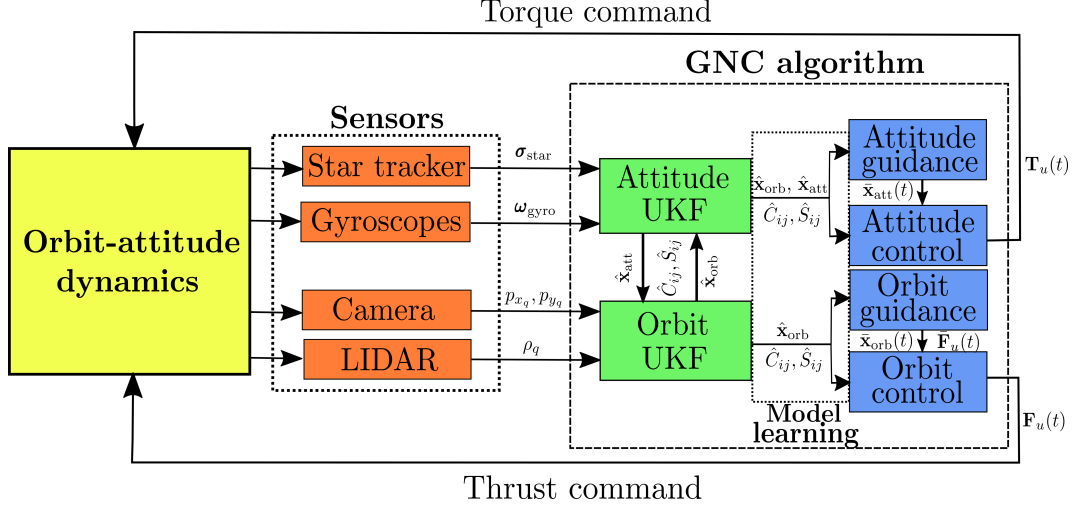
Figure 2: Integrated model-learning GNC scheme.

The attitude dynamics is as follows

$$\mathbf{J}\dot{\boldsymbol{\omega}} = \mathbf{T} - \boldsymbol{\omega} \times \mathbf{J}\boldsymbol{\omega}, \qquad \mathbf{T} = \underbrace{\mathbf{T}_p}_{\text{gravity-gradient}} + \underbrace{\mathbf{T}_u}_{\text{control torque}}, \qquad (10)$$

where $\mathbf{J}$ is the inertia matrix and the external torque $\mathbf{T}$ is composed of the gravity-gradient torque, $\mathbf{T}_p$ and the control torque $\mathbf{T}_u$. In this manuscript, the gravity-gradient torque model is computed assuming a discrete mass distribution. Let define the spacecraft mass distribution through $l_{\max}$ discrete masses m_l ($l = 1 \dots l_{\max}$) placed at $\Delta\mathbf{r}_l$ relative positions with respect to the center of mass $\mathbf{r}$. Then, the gravity-gradient torque computation yields

$$\mathbf{T}_p = \sum_{l=1}^{l_{\max}} m_l \Delta\mathbf{r}_l^B \times \mathbf{F}_g^B(\mathbf{r} + \Delta\mathbf{r}_l, \boldsymbol{\sigma}), \qquad (11)$$

where the term $\mathbf{F}_g^B = \mathbf{R}_O^B(\boldsymbol{\sigma})\left[\mathbf{F}_c(\mathbf{r}) + \mathbf{F}_p(\mathbf{r})\right]$ collects the Keplerian ($\mathbf{F}_c = [-\mu/r^2, 0, 0]^T$) and non-Keplerian gravity. Note that $\mathbf{r} \equiv \mathbf{f}_{\text{orb}}(\mathbf{x}_{\text{orb}})$.

3 INTEGRATED MODEL-LEARNING GNC SCHEME

The proposed GNC architecture is shown in Fig. 2. A camera and a LIDAR are assumed as orbit navigation devices while star-trackers and gyroscopes are employed for attitude determination. The internal data processing of these devices is out of the scope of this work. This manuscript focuses on the GNC algorithms. As such, orbit and attitude UKF work independently with their respective sensors and models since attitude measurements are taken at higher frequencies than orbit ones. However, they periodically exchange their outputs as the camera orientation (orbit) and gravity-gradient torque (attitude) have to be accounted for. The orbit-attitude guidance and control algorithms are MPC-based. Since the filters estimate both the state and the gravity parameters for the guidance and control module, a model-learning predictive control scheme is obtained.

3.1 Asteroid navigation with in-situ gravity estimation

The UKF is employed as the navigation estimation technique. Algorithm 1 shows the UKF steps. The UKF assumes the estimation variable and measurements are normally distributed such that

---

Algorithm 1 (UKF with process noise estimation)

Input: $\boldsymbol{\mu}_0$, $\boldsymbol{\Sigma}_0$, $\mathbf{z}$, $\mathbf{Q}_y$, $\mathbf{Q}_z$

Output: $\boldsymbol{\mu}$, $\boldsymbol{\Sigma}$, $\hat{\mathbf{Q}}_y$

1: Sigma points generation: $\boldsymbol{\chi}^{[k]} = \boldsymbol{\mu}_0 + \mathrm{sgn}(k)\left(\sqrt{(n+\lambda)\boldsymbol{\Sigma}_0}\right)_{|k|}$, $k = -n, \ldots 0 \ldots n$.

2: Process UT: $\boldsymbol{\mu}' = \sum\limits_{k=-n}^{n} w_m^{[k]} \mathbf{g}(\boldsymbol{\chi}^{[k]})$, $\boldsymbol{\Sigma}' = \sum\limits_{k=-n}^{n} w_c^{[k]} \left(\mathbf{g}(\boldsymbol{\chi}^{[k]}) - \boldsymbol{\mu}'\right)\left(\mathbf{g}(\boldsymbol{\chi}^{[k]}) - \boldsymbol{\mu}'\right)^T + \mathbf{Q}_y$.

3: Measurements UT: $\mathbf{Z}^{[k]} = \mathbf{h}(\mathbf{g}(\boldsymbol{\chi}^{[k]}))$, $\hat{\mathbf{z}} = \sum\limits_{k=-n}^{n} w_m^{[k]} \mathbf{Z}^{[k]}$, $\mathbf{S} = \sum\limits_{k=-n}^{n} w_c^{[k]} \left(\mathbf{Z}^{[k]} - \hat{\mathbf{z}}\right)\left(\mathbf{Z}^{[k]} - \hat{\mathbf{z}}\right)^T + \mathbf{Q}_z$

4: Compute Kalman gain: $\mathbf{H} = \sum\limits_{k=-n}^{n} w_c^{[k]} \left(\mathbf{g}(\boldsymbol{\chi}^{[k]}) - \boldsymbol{\mu}'\right)\left(\mathbf{Z}^{[k]} - \hat{\mathbf{z}}\right)^T$, $\quad \mathbf{K} = \mathbf{H}\mathbf{S}^{-1}$.

5: Predict the state and its covariance: $\boldsymbol{\mu} = \boldsymbol{\mu}' + \mathbf{K}(\mathbf{z} - \hat{\mathbf{z}})$, $\quad \boldsymbol{\Sigma} = \boldsymbol{\Sigma}' - \mathbf{K}\mathbf{H}\boldsymbol{\Sigma}'$..

6: Estimate the process noise and its covariance: $\hat{\mathbf{w}} = \mathbf{K}(\mathbf{z} - \hat{\mathbf{z}})$, $\quad \hat{\mathbf{Q}}_y = (1-\alpha)\hat{\mathbf{w}}\hat{\mathbf{w}}^T + \alpha \mathbf{Q}_y$.

$\mathbf{y} \sim N_n(\boldsymbol{\mu}, \boldsymbol{\Sigma})$ and $\mathbf{z} \sim N_m(\mathbf{0}, \mathbf{Q}_z)$ respectively. The state propagation and its mapping to measurements is usually dependant on non-linear functions $\mathbf{g}$ and $\mathbf{h}$. To tackle that, the UKF provides a simplified particle-based approach, named as the unscented transform (UT), in order to obtain the result of applying a non-linear function to a normal distribution. The UT generates $2n+1$ particles (named sigma points) symmetrically distributed with respect to the mean. The non-linear function is applied to the sigma points and the transformed normal distribution is reconstructed by computing the sigma points mean and covariance. In particular, the UT is employed for the process function between measurements $\mathbf{g}$ (step 2), and the subsequent transformation to measurements space $\mathbf{h}$ (step 3). The process and measurements uncertainty is added through the covariance matrices $\mathbf{Q}_y$ and $\mathbf{Q}_z$ respectively. After the previous steps, the Kalman gain is computed using the cross-correlation (step 4). When the measurements $\mathbf{z}$ are available the state and its covariance are predicted (step 5).

The UKF requires tuning of the sigma points spread, the normal distribution reconstruction weights and the process/measurements covariance. The measurements uncertainty $\mathbf{Q}_z$ is usually known as provided by sensors datasheet. On the other hand, the process covariance is unkown since it quantifies the mismatch between truth and model dynamics (which may be time-varying). To overcome that issue, the process noise is recursively updated with the resulting innovation, $(\mathbf{z} - \hat{\mathbf{z}})$, using a fading factor $\alpha \in [0, 1]$ (step 6). Finally, following [10], the spread of sigma points (step 1) and reconstruction weights are mastered by the tuning parameters $\{\theta, \beta, \lambda\}$ such that $w_m^{[0]} = \lambda/(n+\lambda)$, $w_c^{[0]} = w_m^{[0]}(1 - \theta^2 + \beta)$ and $w_c^{[k]} = w_m^{[k]} = 1/[2(n+\lambda)]$, $k \neq 0$.

3.1.1 Orbit filter

The orbit filter provides an estimation of the orbit and the gravity spherical harmonics up to a certain degree and order $n_{\mathrm{orb}} \times n_{\mathrm{orb}}$. Then, the orbit estimation state is

$$\mathbf{y}_{\mathrm{orb}} = [\mathbf{x}_{\mathrm{orb}}^T, C_{ij}, S_{ij}]^T, \quad i = 1 \ldots n_{\mathrm{orb}}, \; j = 1 \ldots n_{\mathrm{orb}}, \tag{12}$$

and the orbit process is represented by the following function

$$\mathbf{g}_{\mathrm{orb}}(\mathbf{y}_{\mathrm{orb}}) = [\varphi_{\mathrm{orb}}^{t,t_0}(\mathbf{x}_{\mathrm{orb},0}, C_{ij}, S_{ij}, \mathbf{F}_u), C_{ij}, S_{ij}]^T, \tag{13}$$

where $\varphi_{\mathrm{orb}}^{t,t_0} : \mathbb{R}^{9 + \sum_{i=2}^{n_{\mathrm{orb}}} 2i+1} \rightarrow \mathbb{R}^6$ is the flow of the MEE GVE ($\mathbf{f}_{\mathrm{GVE}}$) only accounting for the $n_{\mathrm{orb}} \times n_{\mathrm{orb}}$ inhomogeneous gravity and the applied control. The gravity parameters remain invariant along the process.

The orbit measurements are taken by a camera and a LIDAR. These devices track identified features on the asteroid surface, named as landmarks, which are surveyed at a higher orbit phase (out of the scope of this work). Consequently, the set of landmarks positions is known as $\mathbf{r}_q^A$ being q the landmark index. The camera provides the landmark pixel row and column on the camera plane as $\mathbf{p}_q = [p_{x_q}, p_{y_q}]^T$ while the LIDAR provides ranging distance ρ_q between the satellite and the landmark. Assuming a camera pinhole model, the MEE can be mapped to landmarks pixels. First, let express the satellite-landmark relative position, $\boldsymbol{\rho}_q$, in the camera frame

$$\boldsymbol{\rho}_q^C = \mathbf{R}_B^C \mathbf{R}_I^B(\boldsymbol{\sigma}_{B/I})[\mathbf{R}_A^I \mathbf{f}_{\text{orb}}(\mathbf{x}_{\text{orb}}) - \mathbf{r}_q^A], \tag{14}$$

where the spacecraft has to be adequately oriented due to the term $\mathbf{R}_I^B$. Since the camera bore-sight was assumed on the z_C direction, the landmark coordinates on the image plane are $[u_q, v_q] = f_{\text{foc}}[\rho_{x_q}, \rho_{y_q}]/\rho_{z_q}$. The term f_{foc} is the focal length. Then, accounting for the pixel resolution (in terms of pixel width) and its discrete nature, the pixel row and column is given by

$$\mathbf{p}_q = [p_{x_q}, p_{y_q}]^T = [\lfloor u_q/p_{\text{width}} \rfloor, \lfloor v_q/p_{\text{width}} \rfloor]^T. \tag{15}$$

The LIDAR ranging distance directly reads as $\rho_q = \|\boldsymbol{\rho}_q\|_2$. As a limited number of m landmarks can be tracked between UKF calls (due to lighting conditions and feature recognizition algorithm limitations), the orbit measurement is

$$\mathbf{z}_{\text{orb}} = [\mathbf{p}_{q_1}^T, \rho_{q_1}, \ldots \mathbf{p}_{q_m}^T, \rho_{q_m}]^T. \tag{16}$$

3.1.2 Attitude filter

The attitude filter estimates the spacecraft rotational state and the gravity spherical harmonics to a certain degree and order $n_{\text{att}} \times n_{\text{att}}$ (usually, $n_{\text{att}} \leq n_{\text{orb}}$). Then, the attitude estimation state is

$$\mathbf{y}_{\text{att}} = [\boldsymbol{\sigma}^T, \boldsymbol{\omega}^T, C_{ij}, S_{ij}]^T, \quad i = 1 \ldots n_{\text{att}}, \ j = 1 \ldots n_{\text{att}}, \tag{17}$$

and the attitude process function is

$$\mathbf{g}_{\text{att}}(\mathbf{y}_{\text{att}}) = [\varphi_{\text{att}}^{t,t_0}(\boldsymbol{\sigma}, \boldsymbol{\omega}, C_{ij}, S_{ij}, \mathbf{x}_{\text{orb}}, \mathbf{T}_u), C_{ij}, S_{ij}]^T, \tag{18}$$

where $\varphi_{\text{att}}^{t,t_0} : \mathbb{R}^{9+\sum_{i=2}^{n_{\text{orb}}} 2i+1} \to \mathbb{R}^6$ is the attitude kinematics and dynamics flow. Since, the sensors take measurements with respect to the inertial frame, the orientation and angular velocity are referred to that frame within the filter. The body orientation with respect to the orbit frame can be subsequently reconstructed as $\boldsymbol{\sigma} \xrightarrow{-\boldsymbol{\sigma}_{O/I}} \boldsymbol{\sigma}_{B/O}$ where the orbit frame orientation depends on the orbit state. The orbit state estimation is also needed to compute the gravity-gradient torque.

The attitude measurements are assumed to be provided by star-trackers and gyroscopes. In a simplified way, these devices provide direct orientation and angular velocity measurements of the body with respect to the inertial frame, thus

$$\mathbf{z}_{\text{att}} = [\boldsymbol{\sigma}_{B/I}^T, \boldsymbol{\omega}^T]^T. \tag{19}$$

3.2 Model-learning guidance and predictive control

The control goal is to station-keep a circular orbit (which is bounded by definition) while guaranteeing camera line-of-sight with the asteroid surface. In order to achieve these requirements, an orbit-attitude MPC-based guidance and control strategy is presented. The prediction model is recursively updated with the filter gravity parameters estimation. The guidance algorithm generates a reference to be subsequently tracked by a simplified control static program.

3.2.1 Orbit guidance

A circular orbit is achieved if the semi-major axis a is constant and the eccentricity e is null. These variables are expressed in terms of MEE as $a = p/(1 - e^2)$ and $e = \sqrt{f^2 + g^2}$. If the target circular orbit is of $\bar{a}$ radius, then $\{\bar{p}, \bar{f}, \bar{g}\} = \{\bar{a}, 0, 0\}$ (note that the bar denotes the reference). To prescribe these elements, the reference control acceleration cancels the inhomogeneous gravity field perturbation as $\bar{\mathbf{F}}_u(t) = - [F_{\text{grav},r}(\bar{\mathbf{x}}_{\text{orb}}), \ F_{\text{grav},t}(\bar{\mathbf{x}}_{\text{orb}}), \ 0]^T$. Then, the reference GVE yields

$$
\begin{aligned}
\dot{\bar{p}} = &\dot{\bar{f}} = \dot{\bar{g}} = 0, \qquad\qquad & \dot{\bar{h}} = &\sqrt{\frac{\bar{p}}{\mu}} \frac{\bar{s}^2 \bar{F}^O_{\text{grav},n}}{2\bar{w}} \cos \bar{L}, \\
\dot{\bar{k}} = &\sqrt{\frac{\bar{p}}{\mu}} \frac{\bar{s}^2 \bar{F}^O_{\text{grav},n}}{2\bar{w}} \sin \bar{L}, \quad & \dot{\bar{L}} = &\sqrt{\mu \bar{p}} \left(\frac{\bar{w}}{\bar{p}}\right)^2 + \frac{1}{\bar{w}} \sqrt{\frac{\bar{p}}{\mu}} (\bar{h} \sin \bar{L} - \bar{k} \cos \bar{L}) \bar{F}^O_{\text{grav},n}.
\end{aligned}
\tag{20}
$$

This exploits the fact, that for a circular orbit, the radial-tangential motion $(\dot{p}, \dot{f}, \dot{g})$ is independent of the normal elements (h, k, L) and perturbation $(F_{\text{grav},n})$. As such, the normal motion $(\dot{h}, \dot{k}, \dot{L})$ evolves freely and no control is applied in that direction. The reference is generated through numerical integration, over the control horizon, of the ordinary differential equation (ODE) system given by Eq.(20). The propagation yields a time-varying orbit reference

$$
\bar{\mathbf{x}}_{\text{orb}}(t) = [\bar{p}, \ \bar{f}, \ \bar{g}, \ \bar{h}(t), \ \bar{k}(t), \ \bar{L}(t)]^T.
\tag{21}
$$

3.2.2 Attitude guidance

In order to maintain camera pointing to the asteroid surface, a stationary body orientation with respect to the orbit frame has to be ensured. Then, the objective is to keep $\boldsymbol{\sigma}_{B/O} \equiv$ constant. In this case, the required torque to cancel gyroscopic and gravity-gradient terms is neglected, such that

$$
\bar{\mathbf{x}}_{\text{att}}(t) = \left[\bar{\boldsymbol{\sigma}}^T_{B/O}, \ \left(\mathbf{R}(\bar{\boldsymbol{\sigma}}_{B/O}) \boldsymbol{\omega}^O_{O/I}(\bar{\mathbf{x}}_{\text{orb}}(t))\right)^T\right]^T, \quad \bar{\mathbf{T}}_u(t) \approx \mathbf{0},
\tag{22}
$$

where the angular velocity reference has nullifies Eq.(9) attitude kinematics as $\dot{\bar{\boldsymbol{\sigma}}}_{B/O} = \mathbf{0}$. This is a ficticious reference (the control has to cancel its drift) by design but eases computational burden as no integration other than the orbit reference is required in light of Eq.(22).

3.3 Control

This section briefly condenses orbit-attitude controllers for the sake of compactness. Let define the tracking error as $\Delta \mathbf{x}_{(\cdot)}(t) = \mathbf{x}_{(\cdot)}(t) - \bar{\mathbf{x}}_{(\cdot)}(t)$ where the subscript $(\cdot) \equiv \{\text{att, orb}\}$ refers to either the attitude or orbit case. Let denote the control as $\mathbf{u}_{(\cdot)} \equiv \{\mathbf{T}_u, \ \mathbf{F}_u\}$ which refers to the torque (attitude) or control acceleration (orbit) respectively. The subscript $(\cdot)$ is omitted in the sequel.

3.3.1 Continuous tracking problem

The continuous form of the MPC optimization problem is

$$
\begin{aligned}
\min_{\Delta \mathbf{x}(t), \Delta \mathbf{u}(t)} \quad & J = \tfrac{1}{t_f - t_0} \int_{t_0}^{t_f} \left(\gamma \Delta \mathbf{x}^T(t) \mathbf{P}_x \Delta \mathbf{x}(t) + \Delta \mathbf{u}^T(t) \Delta \mathbf{u}(t)\right) dt, \\
\text{s.t.} \quad & \Delta \dot{\mathbf{x}}(t) = \dot{\mathbf{x}}(t, \mathbf{u}(t)) - \dot{\bar{\mathbf{x}}}(t, \bar{\mathbf{u}}(t)), \quad \mathbf{u}(t) = \bar{\mathbf{u}}(t) + \Delta \mathbf{u}(t), \\
& -\mathbf{u}_{\max} \le \mathbf{u}(t) \le \mathbf{u}_{\max}, \\
& \Delta u_n(t) = 0, \quad \text{if} \quad (\cdot) \equiv \text{orb},
\end{aligned}
\tag{23}
$$

where the incremental control $\Delta\mathbf{u}$ has been introduced. The last constraint precludes normal control for the orbit case. The objective function aims to minimize a combination of tracking errors and control effort using $\gamma > 0$ as the weight parameter. The optimal tracking control problem (23) is a non-linear continuous optimization problem with infinite degrees of freedom. Using dynamics linearization and discretization, problem (23) will be reduced into a static quadratic program.

3.3.2 Static control program

Since the goal is to station-keep a reference orbit, the position tracking errors are expected to be low with respect to the orbital radius $\|\Delta\mathbf{r}\|_2/\bar{a} << 1$. Consequently, the gravity acceleration and gravity-gradient torque perturbations can be linearized with respect to the orbit reference such that

$$\Delta\dot{\mathbf{x}}(t) = \mathbf{A}(\bar{\mathbf{x}}(t), \bar{\mathbf{u}}(t))\Delta\mathbf{x}(t) + \mathbf{B}(\bar{\mathbf{x}}(t), \bar{\mathbf{u}}(t))\Delta\mathbf{u}(t) + \Delta\dot{\mathbf{x}}(t). \tag{24}$$

Equation (24) represents a linear time-varying system (LTV) due to the time-varying reference. Note that $\Delta\dot{\mathbf{x}}(t) = \dot{\mathbf{x}}(\bar{\mathbf{x}}(t), \bar{\mathbf{u}}(t)) - \dot{\mathbf{x}}(t)$ is the reference drift which accounts for a fictitious guidance reference. A LTV system admits a general solution in terms of the state transition matrix $\mathbf{\Phi}$

$$\Delta\mathbf{x}(t) = \mathbf{\Phi}(t, t_0)\Delta\mathbf{x}_0 + \int_{t_0}^{t} \mathbf{\Phi}(t, \tau)\mathbf{B}(\tau)\Delta\mathbf{u}(\tau)d\tau + \Delta\bar{\mathbf{x}}(t), \tag{25}$$

where the transition matrix is obtained by integration of the following ODE

$$\dot{\mathbf{\Phi}}(t, t_0) = \mathbf{A}(\bar{\mathbf{x}}(t))\mathbf{\Phi}(t, t_0), \quad \mathbf{\Phi}(t_0, t_0) = \mathbf{I}. \tag{26}$$

Note that for both orbit-attitude cases, Eq.(26) is an ODE system with 36 differential equations.
Using the general solution of Eq.(25), the continuous control problem (23) can be discretized as follows. Let divide the control horizon into N sampling intervals of duration $\Delta t = (t_f - t_0)/N$. Then, the tracking error equation Eq.(25) is evaluated at discrete instants $t_k = t_0 + k\Delta t$ ($k = 1 \ldots N$) while the control is assumed constant, $\mathbf{u}_k$, during the sampling interval k. Under the previous considerations, a finite static program is posed as

$$\begin{aligned}
\min_{\Delta\mathbf{u_k}} \quad & J = \sum_{k=1}^{N} \left(\gamma\Delta\mathbf{x}_k^T\mathbf{P}_x\Delta\mathbf{x}_k + \Delta\mathbf{u}_k^T\Delta\mathbf{u}_k\right), \\
\text{s.t.} \quad & \Delta\mathbf{x}_k = \mathbf{\Phi}_{k,0}\Delta\mathbf{x}_0 \\
& + \sum_{i=1}^{k} \mathbf{\Phi}_{k,i} \left(\int_{t_{i-1}}^{t_i} \mathbf{\Phi}(t_i, \tau)\mathbf{B}(\tau)d\tau\right) \Delta\mathbf{u}_i + \Delta\bar{\mathbf{x}}_k, \\
& -\mathbf{u}_{\max} \leq \bar{\mathbf{u}}_k + \Delta\mathbf{u_k} \leq \mathbf{u}_{\max}, \\
& \Delta u_{n,k} = 0 \quad \text{if} \quad (\cdot) \equiv \text{orb},
\end{aligned} \tag{27}$$

which is a QP problem with $3N$ decision variables.

4 NUMERICAL RESULTS

This section presents the model-learning predictive controller numerical results as well as a comparison with respect to a non-learning controller where the filter does not communicate the model update to the MPC guidance and control. The simulations are carried out in MATLAB using a i7-8700 CPU 3.2 GHz processor.

4.1 Scenario parameters

The target asteroid is 433 Eros. This small body was accurately characterized during the NEAR Shoemaker mission. Eros has a gravitational parameter of $\mu = 4.4628 \cdot 10^5 \text{ m}^3/\text{s}^2$, a rotation period of $T = 5.27$ h around its major inertia axis and its inhomogeneous gravity field is known up to 15×15 degree and order [24]. These coefficients are normalized with $R_e = 16$ km and are employed to simulate the truth dynamical environment. In the asteroid inertial frame, the Sun position is assumed as $\mathbf{r}_\odot = [1.46, 0, 0]^T$ AU with respect to the asteroid center of mass.

The satellite has a camera with 2048×2048 pixels resolution, a $30°$ field of view, and 300 mm of focal length. It is assumed that at most $m = 3$ landmarks can be tracked, betweeen filter calls. These are chosen as the ones with the higher relative elevation with respect to the camera boresight ($z_C \equiv -x_B$). A set of 522 surface landmarks positions from Eros mission data [24] is assumed as known. Table 1 shows the considered sensors noises datasheet (the star tracker noise is introduced via the rotation angle θ_{rot}).

Table 1: Sensors datasheet

Sensor	Variable	Bias	1-σ noise
Camera	$\mathbf{p}_q$	$[0,0]^T$ px	$[0.5, 0.5]^T$ px
LIDAR	ρ_q	0 m	5 m
Star tracker	θ_{rot}	0 arcsec	10 arcsec
Gyroscopes	$\boldsymbol{\omega}_{\text{gyro}}$	$[5,5,5]^T$ °/h	$[0.05, 0.05, 0.05]^T$ °/h

The control acceleration and torque bounds are taken as $\mathbf{F}_{u_{\max}} = [1, 1, 1]^T \text{ cm/s}^2$ and $\mathbf{T}_{u_{\max}} = [1, 1, 1]^T \text{ N} \cdot \text{cm}$. Since a continuous acceleration is always applied, the specific impulse is taken as the one of an electric thruster, $I_{sp} = 2900$ s. The satellite mass is $m = 1000$ kg and its principal inertias are $\{J_{11}, J_{22}, J_{33}\} = \{2000, 16400, 17600\} \text{ kg} \cdot \text{m}^2$. The coefficient of reflectivity and SRP exposed area are $C_R = 1.4$ and $A = 10 \text{ m}^2$ respectively.

Regarding GNC tuning parameters, the filters spherical harmonics estimation degree and order is $\{n_{\text{orb}}, n_{\text{att}}\} = \{4, 2\}$. The UKF tuning parameters are taken as $\{\alpha, \theta, \beta, \lambda\} = \{0.98, 10^{-3}, 2, (\theta^2 - 1)n\}$ being n the dimension of the extended state (27 for orbit and 14 for attitude). Regarding sampling rates the attitude and orbit UKF are executed each 3.6 s and 36 s respectively. The attitude filter sampling rate is one order of magnitude higher than the orbit as its sensors takes measurements with faster frequencies. The guidance and control algorithm parameters (control horizon, discretization intervals, interval duration and tracking error weight) are stated in Table 2.

Table 2: Guidance and control algorithm parameters.

	Control horizon [min]	$N \, [-]$	$\Delta t \, [\text{s}]$	$\gamma \, [-]$
Attitude	6	10	36	10^3
Orbit	240	40	360	10^3

For all the simulations, an accurate navigation fix is considered available, thus $\mathbf{x}_{\text{orb}}(t_0) = \hat{\mathbf{x}}_{\text{orb}}(t_0)$; $\mathbf{x}_{\text{att}}(t_0) = \hat{\mathbf{x}}_{\text{att}}(t_0)$. However, gravity inhomogeneities are completely unknown as $\hat{C}_{ij} = \hat{S}_{ij} = 0$. The initial 1-sigma uncertainty on all the gravity parameters is taken as $5 \cdot 10^{-3}$. The state initial uncertainty follows a diagonal covariance matrix such that $\boldsymbol{\Sigma}_{\text{orb},11}(t_0) = 5^2$, $\boldsymbol{\Sigma}_{\text{orb},ii}(t_0) = (5 \cdot 10^{-6})^2$ for $i = 2, \dots 6$ while $\boldsymbol{\Sigma}_{\text{att},ii}(t_0) = (10^{-6})^2$ for $i = 1, 2, 3$ and $\boldsymbol{\Sigma}_{\text{att},ii}(t_0) = (10^{-8})^2$ for $i = 4, 5, 6$.

4.2 Simulations

The reference orbit is defined by $\{\bar{a}, \bar{e}\} = \{34 \text{ km}, 0\}$. To assess the efficiency of the learning-based control methodology, several initial inclinations $i_0 = \{30°, 60°, 90°, 120°, 150°\}$ are combined with these initial semi-major axes $a_0 = \{33, 33.5, 34, 34.5, 35\}$ km. The initial orbit is circular, $e_0 = 0$ and the other elements are $\omega_0 = \Omega_0 = \nu_0 = 0°$. The previous combination provides 25 cases for each controller. The duration of each scenario is two weeks.

Figure 3 shows the satellite trajectories, relative to the asteroid, for different initial inclinations. It can be observed that no escape or collision with the asteroid arises. Figure 4 shows the orbital radius evolution, for both controllers, of the polar orbit scenario with different initial conditions. It can be deduced that the learning-based MPC achieves a more accurate reference tracking than the non-learning MPC scheme.

The numerical comparison of both control strategies is shown in Tables 3-4 for orbit-attitude control performance. The reported values average the five scenarios resulting from applying different initial conditions for each inclination. The orbit control metrics are fuel consumption (m_F), average and maximum absolute tracking errors (ΔR and $\Delta R_{\max}$). The attitude control metrics are the average torque (T_U) and the average orientation error in terms of pitch, roll and yaw angles ($\Delta \mathbf{\Theta}$). The orbit results, see Table 3, shows that the learning-based MPC control can provide up to a 29% increase ($i_0 = 90°$) or an 8% ($i_0 = 30°$) decrease in fuel consumption. However, the developed controller reduces tracking errors between a 7% to a 91%, with respect to the non-learning MPC, while also guaranteeing the error is below 1 km. The attitude results, see Table 4, shows a decreasing trend, ranging between 9-19%, in terms of torque demands for the learning-based MPC with respect to the non-learning MPC. This does not provoke any loss of accuracy in terms of the orientation angles. Nonetheless, it is observed that the pitch presents a slight offset ($\approx 1.55°$) for all simulations.

An example of orbit filter estimation in terms of position error and relevant gravity parameters ($|C_{ij}|, |S_{ij}| > 2 \cdot 10^{-3}$) is shown in Fig.5-6. The position error shows a decreasing trend as the gravity estimation converges. The average position error decreases from 23.6 m along the first week to 14.4 m during the second week. Gravity parameters are accurately estimated for second order gravity terms ($<2\%$ final error for all the parameters) while third and fourth order gravity show significant discrepancies with truth values. This may be caused by the absorption of unmodelled dynamics such as higher order gravity and solar perturbations.

Table 3: Orbit control performance of learning-based MPC and non-learning MPC

Simulation	Learning-based MPC			Non-learning MPC		
	m_F [kg]	ΔR [m]	$\Delta R_{\max}$ [m]	m_F [kg]	ΔR [m]	$\Delta R_{\max}$ [m]
$i_0 = 30°$	1.7943	159.17	864.67	1.9668	1280.5	1829.2
$i_0 = 60°$	1.3547	264.84	983.92	1.2640	284.90	921.90
$i_0 = 90°$	1.4034	316.38	971.50	1.0903	797.04	1247.9
$i_0 = 120°$	1.3378	167.35	840.81	1.1330	241.13	820.26
$i_0 = 150°$	1.7447	129.85	847.83	1.6742	1390.8	1681.5

The computational times of the GNC algorithms have been measured for the learning-based MPC. The attitude and orbit filters average execution times are, 47.7 ms and 71.4 ms respectively (being the peak of 51.9 ms and 77.1 ms). On the other hand, attitude and control guidance and control modules average execution times yields 1.53 s and 3.76 s respectively (being the peak of 1.65 s and 5.11 s). These are promising results in terms of demonstrating the potential concept autonomy.
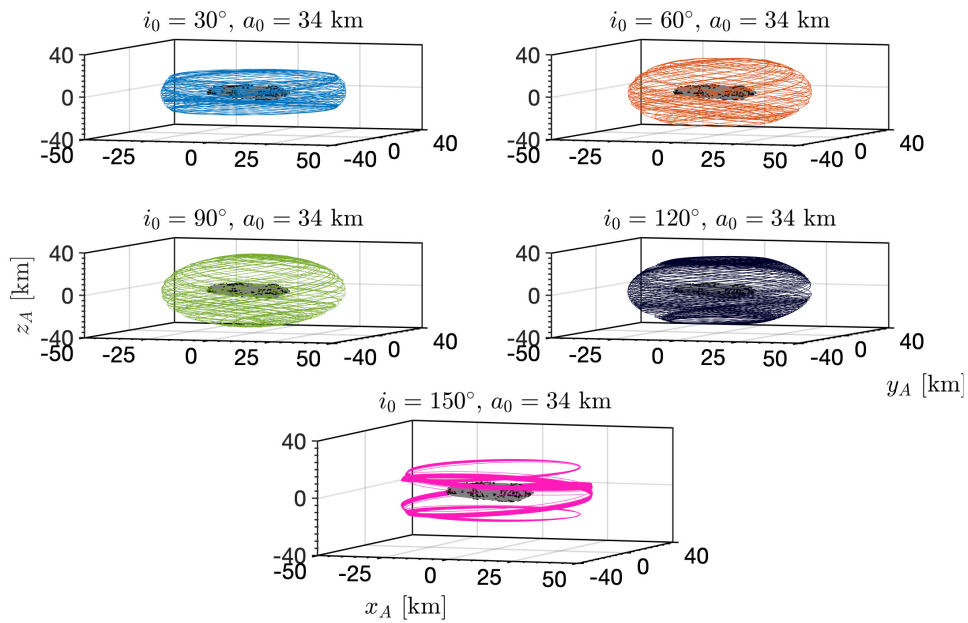
Figure 3: Trajectories in the asteroid frame for learning-based MPC. Black dots: landmarks.
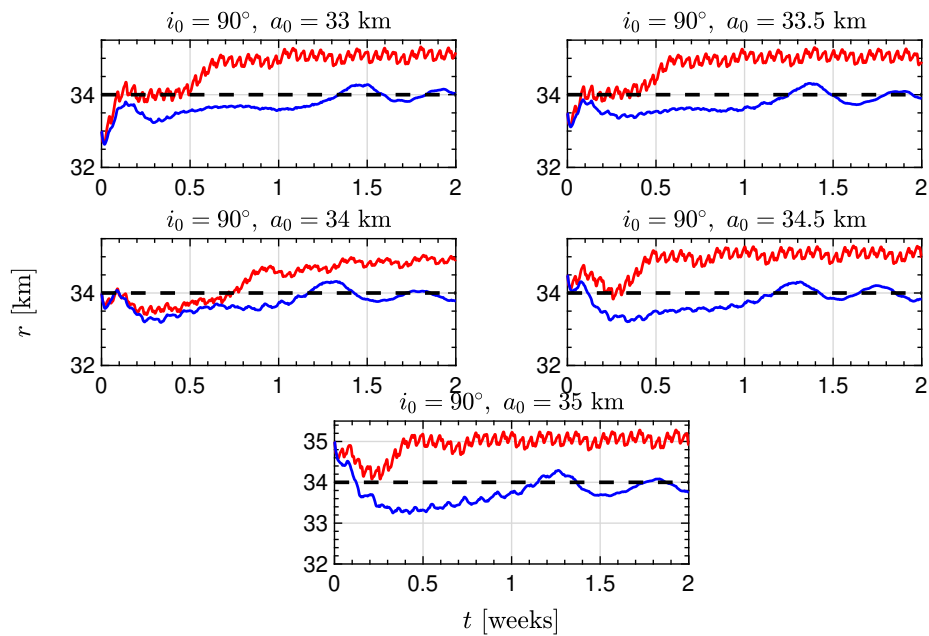

Figure 4: Orbital radius for the polar orbit case. Black-dashed: reference; blue: learning-based MPC; red: non-learning MPC.

Table 4: Attitude control performance of learning-based MPC and non-learning MPC

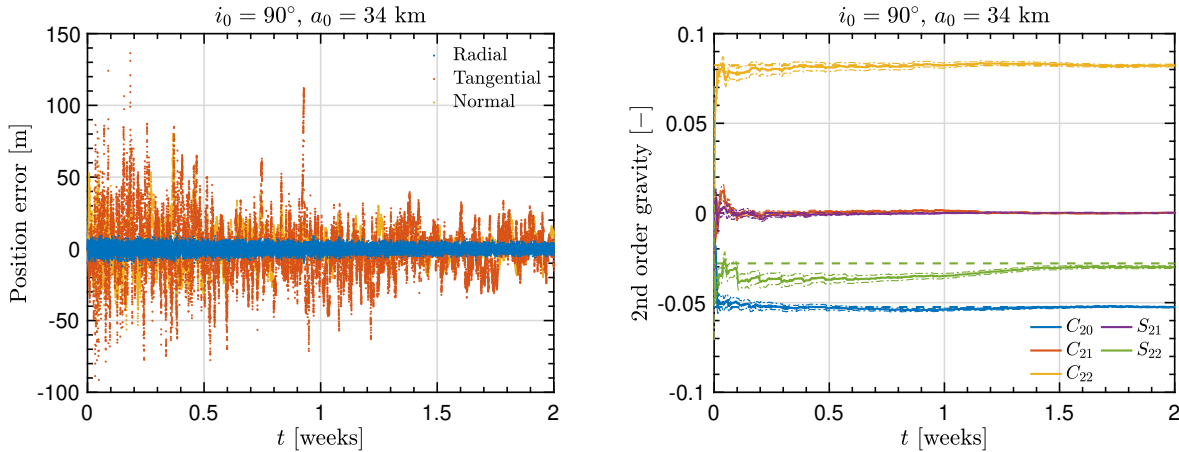| Simulation	Learning-based MPC		Non-learning MPC	
	T_U [mN·m]	$\Delta\Theta$ [°]	T_U [mN·m]	$\Delta\Theta$ [°]
$i_0 = 30°$	0.6199	$[1.55, 0.02, 0.05]^T$	0.7634	$[1.59, 0.02, 0.04]^T$
$i_0 = 60°$	0.5739	$[1.55, 0.02, 0.05]^T$	0.6556	$[1.59, 0.02, 0.04]^T$
$i_0 = 90°$	0.4986	$[1.54, 0.02, 0.05]^T$	0.5481	$[1.59, 0.02, 0.04]^T$
$i_0 = 120°$	0.5928	$[1.54, 0.02, 0.05]^T$	0.6894	$[1.58, 0.02, 0.05]^T$
$i_0 = 150°$	0.6248	$[1.54, 0.02, 0.05]^T$	0.7777	$[1.58, 0.02, 0.04]^T$

Figure 5: Learning-based MPC position error (*left*) and second-order gravity estimation (*right*). Dashed≡truth; solid≡estimation; dot-dashed≡1-σ uncertainty.

5 CONCLUSIONS

An integrated model-learning predictive GNC strategy for orbit-attitude station-keeping in the vicinity of an asteroid has been presented. The develop algorithmic architecture combines unscented Kalman filtering with model predictive control. The main source of model uncertainty comes from the asteroid gravity field inhomogeneities which can not be sensed until the satellite is close enough to the asteroid. The proposed concept has the potential to undertake gravity estimation, at a minimal extent, while guaranteeing the satellite lies in a closed orbit. This may enable further operations such as transferring the satellite to a frozen orbit in terms of second order gravity.

The learning-based MPC has been compared to a non-learning MPC demonstrating that, in exchange for a slight increase in fuel consumption, a more accurate orbit tracking is always achieved. Moreover, the attitude control demands are always lower for the learning-based control without loss of accuracy. Regarding future work, recent asteroid exploration works, such as [14], are analyzing the potential benefits of using multiple spacecraft mission concepts instead of the considered single satellite configuration. Extending this scheme to a multiple satellite mission is left as future work.

REFERENCES

[1] J. C. Castillo-Rogez, M. Pavone, J. A. Hoffman, and I. A. D. Nesnas, "Expected science return of spatially-extended in-situ exploration at small solar system bodies," in *2012 IEEE Aerospace*
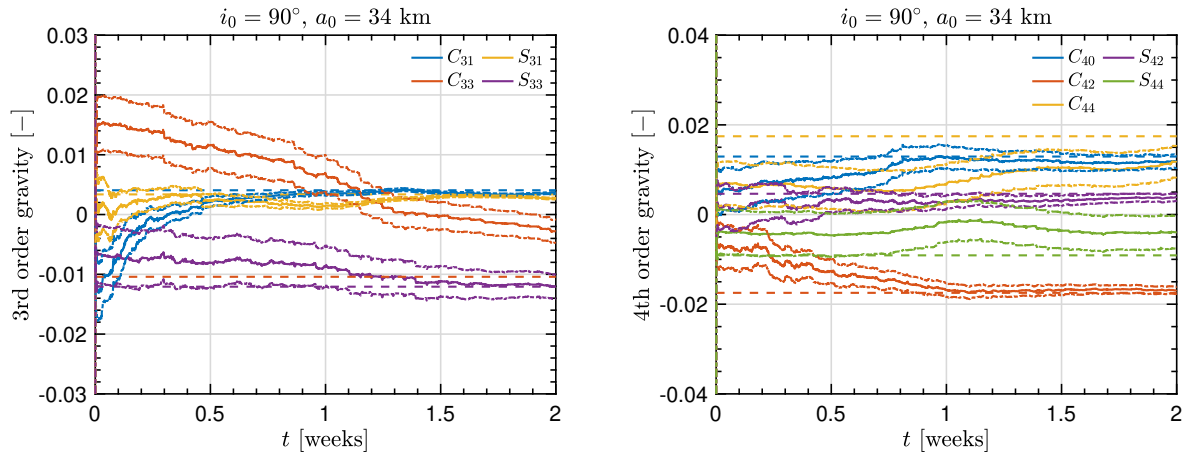
Figure 6: Learning-based MPC third-order gravity (*left*) and fourth-order gravity estimation (*right*). Dashed≡truth; solid≡estimation; dot-dashed≡1-σ uncertainty..

Conference, March 2012, pp. 1–15.

[2] M. Ceccaroni and J. Biggs, "Analytic perturbative theories in highly inhomogenous gravitational fields," *Icarus*, vol. 224, no. 1, pp. 74–85, June 2013.

[3] D. J. Scheeres, "Orbit mechanics about asteroids and comets," *Journal of Guidance, Control, and Dynamics*, vol. 35, no. 3, pp. 987–997, 2012.

[4] Y. Jiang and H. Baoyin, "Periodic orbit families in the gravitational field of irregular-shaped bodies," *The Astronomical Journal*, vol. 152, no. 5, pp. 137–147, 11 2016.

[5] I. Jean, A. K. Misra, and A. Ng, "Solar radiation pressure–compatible trajectories in the vicinity of a binary asteroid," *Journal of Guidance, Control, and Dynamics*, vol. 42, no. 6, pp. 1319–1329, 2019.

[6] E. F. Camacho and C. Bordons, *Model Predictive Control*, 2nd ed. London: Springer-Verlag, 2004, ch. 9, pp. 249–287.

[7] M. Tavakoli and N. Assadian, "Model predictive orbit control of a low earth orbit satellite using gauss variational equations," *Proceedings of the Institution of Mechanical Engineers, Part G: Journal of Aerospace Engineering*, vol. 228, no. 13, pp. 2385–2398, 2014.

[8] S. Hesar, J. Parker, J. McMahon, and G. Born, "Small body gravity field estimation using liaison supplemented optical navigation," in *36th AAS Guidance and Control conference*, Breckenridge, United States of America, 2015.

[9] J. D. Biggs and E. Ciccarelli, "In-situ tracking of a solar sail's characteristic acceleration using a robust active disturbance estimator," in *5th International Symposium on Solar Sailing*, Aachen, Germany, August 2019.

[10] E. Wan and R. Merwe, "The unscented kalman filter for nonlinear estimation," in *Adaptive Systems for Signal Processing, Communications, and Control Symposium*, Alberta, Canada, 2000.

[11] M. Vetrisano and M. Vasile, "Autonomous navigation of a spacecraft formation in the proximity of an asteroid," *Advances in Space Research*, vol. 57, no. 8, pp. 1783–1804, 2016.

[12] A. Dietrich and J. W. McMahon, "Orbit Determination Using Flash Lidar Around Small Bodies," *Journal of Guidance, Control, and Dynamics*, vol. 40, no. 3, pp. 650–665, 2017.

[13] J. Gil-Fernandez and G. Ortega-Hernando, "Autonomous vision-based navigation for proximity operations around binary asteroids," *CEAS Space Journal*, vol. 10, pp. 287–294, 2018.

[14] N. Stacey and S. D'Amico, "Autonomous swarming for simultaneous navigation and asteroid characterization," in *AAS/AIAA Astrodynamics Specialist Conference*, Snowbird, United States of America, 2018.

[15] D. Wibben and R. Furfaro, "Integrated guidance and attitude control for asteroid proximity operations using higher order sliding modes," in *AIAA/AAS Astrodynamics Specialist Conference*, Minneapolis, United States of America, 2012.

[16] B. Gaudet, R. Linares, and R. Furfaro, "Six degree-of-freedom body-fixed hovering over unmapped asteroids via lidar altimetry and reinforcement meta-learning," *Acta Astronautica*, vol. 172, pp. 90–99, 2020.

[17] B. Wie, *Space Vehicle Dynamics and Control*, 2nd ed., ser. AIAA Education Series. Reston, VA: AIAA, 2008, chapter 2, pp. 386-390.

[18] Y. Wang and S. Xu, "Attitude stability of a spacecraft on a stationary orbit around an asteroid subjected to gravity gradient torque," *Celestial Mechanics and Dynamical Astronomy*, vol. 115, pp. 333–352, 04 2013.

[19] L. Hewing, K. P. Wabersich, M. Menner, and M. N. Zeilinger, "Learning-based model predictive control: Toward safe learning in control," *Annual Review of Control, Robotics, and Autonomous Systems*, vol. 3, no. 1, pp. 269–296, 2020.

[20] M. J. H. Walker, B. Ireland, and J. Owens, "A set of modified equinoctial orbit elements," *Celestial Mechanics*, vol. 36, pp. 409–419, 1985.

[21] G. Balmino, "Gravitational potential harmonics from the shape of an homogeneous body," *Celestial Mechanics and Dynamical Astronomy*, vol. 60, pp. 331–364, 1994.

[22] K. C. Howell, D. J. Grebow, and Z. P. Olikara, "Design using gauss' perturbing equations with applications to lunar sourh pole coverage," in *17th AAS/AIAA Spaceflight Mechanics Meeting*, Sedona, United States of America, January 2007.

[23] H. Schaub and J. L. Junkins, "Stereographic Orientation Parameters for Attitude Dynamics: A Generalization of the Rodrigues Parameters," *Journal of the Astronautical Sciences*, vol. 44, no. 1, pp. 1–19, 1996.

[24] A. Konopliv, J. Miller, W. Owen, D. Yeomans, J. Giorgini, R. Garmier, and J.-P. Barriot, "A global solution for the gravity field, rotation, landmarks, and ephemeris of eros," *Icarus*, vol. 160, no. 2, pp. 289–299, 12 2002.